

Leveraging Epsilon Near Zero phenomena for on-chip photonic modulation

Arun Mambra,* Ravi Pant, and Joy Mitra†

School of Physics, Indian Institute of Science Education and Research Thiruvananthapuram, Kerala, India

(Dated: March 10, 2025)

Epsilon-near-zero (ENZ) systems exhibit unconventional electromagnetic response close to their zero permittivity regime. Here, we explore the ability of ultrathin ENZ films to modulate the transmission of radiation from an underlying quantum emitter through active control of the carrier density of the ENZ film. The achievable on/off switching ratio is shown to be constrained by the material's loss parameter, particularly in the ENZ regime, where transmissivity increases with higher material loss. The finite loss in real materials limit the more extraordinary potential of ideal near-zero-index systems. Along with an in-depth discussion on the material parameters vis-a-vis the underlying physics, this work provides avenues to overcome the shortcomings of finite loss in real materials. These findings are intended to guide materials development and offer valuable insights for designing on-chip optical modulators and beam steering devices operating in the near-infrared regime.

I. INTRODUCTION

Metamaterials and metasurfaces have unlocked novel strategies for shaping light using plasmonic resonances interlayer interactions, etc., with applications in imaging, sensing, cloaking, spectroscopy, and energy harvesting [1, 2]. A majority of the above functionalities rely on far-field interference effects which excludes their exploitation for nano-photonic applications. The demands of nano-photonics has driven research in areas like nanoscale light sources and optical elements [3, 4], and crucially in exploring novel optical materials. In recent years, exploration of epsilon near zero (ENZ) properties in continuous media, especially in doped semiconductors has rejuvenated the field. ENZ systems exhibit unique, non-trivial optical properties close to their ENZ wavelength (λ_{ENZ}), at which the real part of the material's relative permittivity ($\epsilon = \epsilon' + i\epsilon''$) goes to zero and the ENZ's optical response transitions between dielectric ($\epsilon' > 0$) and metallic ($\epsilon' < 0$). The ENZ regime ($|\epsilon'| < 1$) exhibit properties like enhanced optical nonlinearities [5, 6], super coupling [7], perfect absorption [8], directional emission [9, 10], slow light [11] and even optical levitation [12]. While some of these properties have been observed in metamaterials [9, 13], their demonstration in homogeneous systems such as degenerately doped semiconductors [14], conducting polymers [10, 15], and polaritonic dielectric materials [8] offer exciting opportunities to explore and exploit ENZ phenomena in extending optical and photonic applications from the micron scale to the nanoscale [16]. Ideal loss-less ENZ systems [17–19] would exhibit properties like infinite phase velocity with zero group velocity [20, 21] in their ENZ regime, which spatially maps electrodynamics to an electrostatic limit. It effectively decouples the temporal and spatial response, disentangling the electric and magnetic components [17, 22–24]

and thus would exhibit perfect reflection and infinite impedance to wave propagation. Though the more extreme consequences are muted in real systems, due to the finite loss (i.e. non-zero ϵ'' and κ), the effects may be leveraged for manipulation of light, especially in the nanoscale.

Here, we investigate the potential of an ultrathin ENZ film with finite loss to achieve on/off control of transmission of radiation from an underlying quantum emitter and its spatio-temporal modulation. This is enabled by dynamically modulating the carrier density of the ENZ film via electric gating that tunes its dielectric properties, including the λ_{ENZ} . Transmission is shown to minimise when the emitter wavelength matches λ_{ENZ} , at which the ENZ film's loss parameter is, paradoxically, shown to aid transmission and thus reduce the achievable transmission on/off ratio. The shortcomings posed by the finite material loss may be offset by increasing the accumulation or depletion length as a fraction of the ENZ film thickness, which is constrained by the carrier density. A straightforward multilayer design is proposed to increase the effective screening length while maintaining the flexibilities of dynamic control. Finally, a compact device architecture for on-chip beam steering is presented, leveraging phase modulations afforded by locally gated ultrathin ENZ film. The results provide key insights into the design and development of nanoscale optical modulators using ENZ systems, paving the way for their integration into on-chip photonic circuits.

II. MATERIALS AND METHODS

Table I lists homogeneous materials that exhibit an ENZ regime, classified as 'free carrier' and 'phononic' based on the underlying origin of the materials' ϵ' going to zero. The 'free carrier' basket include metals, semiconductors and conducting polymers in which the ENZ regime arises due to the collective response of their free carriers, both electrons and holes. The dielectric properties of such systems are well described by the Drude-

* itsmearun18@iisertvm.ac.in

† j.mitra@iisertvm.ac.in

	Material	$\lambda_{ENZ}(\mu m)$	ϵ'' at λ_{ENZ}	Ref
free carrier	Al	0.083	0.03	[25]
	Na	0.23	0.003	[26]
	ITO	1.2 - 2.5	0.3 - 0.8	[14]
	CdO*	1.9	0.14	[8]
	ZnO(Al)*	1.2 - 2	0.29 - 0.8	[27, 28]
	Ga-ZnO	1.19	0.31	[28]
	LABSO	1.44	0.45	[29]
	PEDOT:PSS*	0.65 - 1.7	0.3 - 0.9	[15, 30]
	TDBC	0.4	0.16	[31]
HTJSq	0.52	0.17	[31]	
phononic	SiO ₂	8.143	0.46	[8]
	SiC	10.3	0.03	[28]
	AlN	11.111	0.02	[32]
	Si ₃ N ₄	9.6	0.35	[33]
	Al ₂ O ₃	10.6	0.62	[33]
	SrTiO ₃	12.68, 21.05	0.24, 0.35	[34]
	hBN	6.2 , 12.35 [⊥]	0.08 , 0.05 [⊥]	[35, 36]

TABLE I. Reported ENZ materials and their ϵ'' values at λ_{ENZ} . "*" denotes doping.

Lorentz model, where the free carrier density (N_c) determines the λ_{ENZ} that typically lies between the ultraviolet to the near IR. Fig. 1 plots the real and imaginary components of the refractive index ($\tilde{n} = n + i\kappa$) for ITO, doped CdO and PEDOT:PSS, with the vertical dashed lines identifying the respective λ_{ENZ} . The corresponding dielectric constants are shown in supplementary material (SM) fig. S1 [37], in which the ENZ regimes ($|\epsilon'| < 1$) are identified with colored bands. The ‘phononic’ group include oxides (SiO₂, Al₂O₃), nitrides (AlN) and layered 2D materials like hBN, in which the ENZ regime originates from phonon polaritons and typically have λ_{ENZ} in the mid-IR range, as shown in table I. The present study focuses on the ‘free carrier’ ENZ materials though the physical insights gained into their functionalities in the ENZ regime, are broadly applicable to all homogeneous ENZ media.

Following the Drude model, the relative permittivity of free carrier systems is given by $\epsilon(\omega) = \epsilon_\infty - \omega_p^2 / (\omega^2 + \gamma^2) + i(\omega_p^2 \gamma / \omega(\omega^2 + \gamma^2))$, where three material specific parameters, ϵ_∞ : the high frequency relative permittivity, ω_p : the plasma frequency and γ : the collision rate or damping parameter determine the system’s optical response. The dependence of λ_{ENZ} on N_c as $\lambda_{ENZ} = 2\pi c / \sqrt{\omega_p^2 / \epsilon_\infty - \gamma^2}$ provides a straightforward control over the optical properties of ‘free carrier’ ENZ materials both via chemical doping [8, 14] and electrostatic gating [38, 39], which directly controls N_c . A commercial finite element method (FEM) modeling software COMSOL Multiphysics[®] 5.3a

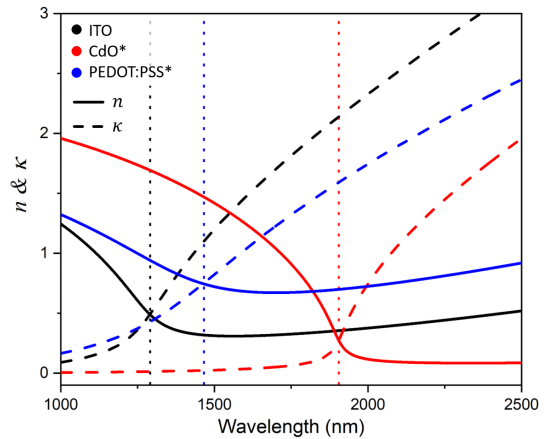


FIG. 1. Real and imaginary parts of the refractive index of ITO, CdO and PEDOT:PSS. Vertical lines denote the λ_{ENZ} , where $n = \kappa$.

was used to conduct the simulations of light-matter interaction in ENZ media. The dipole emitter sources have been defined as current dipoles with emission wavelength (λ_{em}) = 1600 nm. The optical properties of the ENZ material were defined using the Drude model parameters, $\epsilon_\infty = 3.9$; $\gamma = 10^{10}$ Hz - 10^{14} Hz and variable N_c such that λ_{ENZ} lies in the range 1340 nm – 1860 nm. The semiconductor and wave-optics modules of the simulation package were coupled to simulate solutions to the electromagnetic wave equation due to change in dielectric properties of the ENZ system due to electric gating. Further details regarding the simulation domain and geometry of the models along with the boundary conditions, the optimized mesh and material properties used are available at SM section S2 [37].

III. RESULTS AND DISCUSSION

A. Dipole in unbounded ENZ media

The physical manifestations of light-matter interactions in the ENZ regime are discussed through the example of a point dipole emitter, encapsulated in a spherical vacuum bubble (diameter 50 nm), embedded within an unbounded ENZ medium. The simulated electric field lines around the dipole ($\vec{p} = p_o \sin(\omega_{em} t) \hat{i}$), with its free-space emission wavelength $\lambda_{em} = 1600$ nm and $\omega_{em} = 2\pi c / \lambda_{em}$, are shown in fig. 2. The false colored background of the plots correspond to $\log(|\vec{E}|)$ as depicted by the colorbar. The ENZ media is described by the Drude model parameters, $\gamma = 10^{10}$ Hz with a variable N_c such that λ_{ENZ} varies from 1344 nm to 1856 nm. At the dipole emission wavelength (λ_{em}), the ENZ media would respond like a dielectric for $\lambda_{ENZ} > \lambda_{em}$ and like a metal for $\lambda_{ENZ} < \lambda_{em}$. Thus for $\lambda_{ENZ} = 1856$ nm and 1625 nm, the ENZ media is a dielectric with $\epsilon' > 0$ and radiative dipolar modes are evidenced as shown in

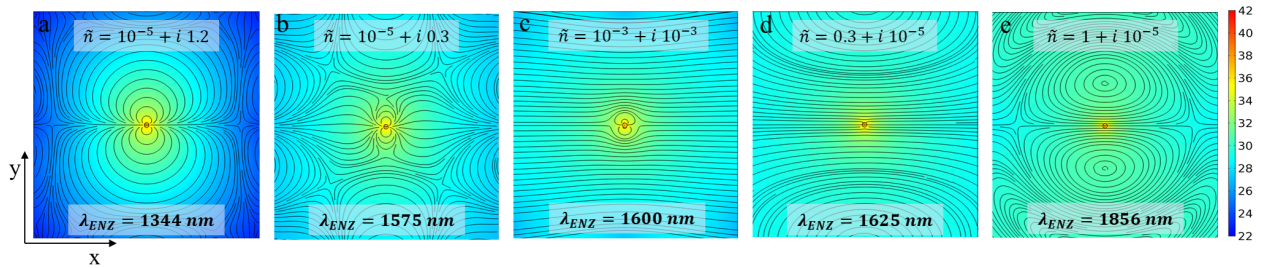


FIG. 2. Electric field lines around a dipole oscillator, radiating at $\lambda_{em} = 1600$ nm, embedded in ENZ media with (a) and (b) $\lambda_{ENZ} < \lambda_{em}$, (c) $\lambda_{ENZ} = \lambda_{em}$ and (d) and (e) $\lambda_{ENZ} > \lambda_{em}$. λ_{ENZ} and the \tilde{n} at 1600 nm are mentioned individually. Background color represents $\log(|\vec{E}|)$ as per the colorbar. Plot dimensions: $2.5 \mu\text{m} \times 2.5 \mu\text{m}$.

figs. 2d and 2e. The values of \tilde{n} for the ENZ film at 1600 nm, listed in the figures, indicate that reduction of λ_{ENZ} towards λ_{em} is accompanied by the decrease in n at 1600 nm, which leads to spatial stretching of the field pattern. For $\lambda_{ENZ} \approx \lambda_{em}$, $n = \kappa \simeq 10^{-3}$ and spatially the electric field lines mimic that of a static dipole, as shown in fig. 2c and SM fig. S3 [37]. For $\lambda_{em} > \lambda_{ENZ}$, an ideal loss-less ENZ ($\epsilon' < 0$ and $\epsilon'' = 0$) would respond as a lossy material with a purely imaginary $\tilde{n} = i\sqrt{\epsilon'}$, causing strong attenuation that prohibits propagation, but may sustain non-radiative modes in ENZ regime[20, 21]. However, the finite loss in real ENZ systems ensure that the n remains non-zero at wavelengths greater than λ_{ENZ} , thus allowing propagation. Figs. 2a-b show the electric field for two cases with progressively higher N_c with $\lambda_{ENZ} = 1575$ and 1344 nm, that renders the ENZ system metallic at 1600 nm. Note that both cases show with a small yet finite n at λ_{em} , with κ increasing as λ_{ENZ} decreases, resulting in stronger attenuation of the propagating modes. Variation in the dipole power radiated across the ENZ media as its λ_{ENZ} (i.e. N_c) is decreased, such that the ENZ medium changes from a dielectric to metallic behavior at 1600 nm is shown in fig. 3a, for two different values of γ . For the lower value of $\gamma = 10^{10}$ Hz, the radiated power is highest if the ENZ medium is a dielectric and decreases with λ_{ENZ} , reaching a minimum for $\lambda_{ENZ} = \lambda_{em}$. For $\lambda_{ENZ} < \lambda_{em}$, the radiated power initially increases but then diminishes due to stronger dissipation in the medium. Under higher damping ($\gamma = 10^{13}$ Hz), the radiated power is lower in both the dielectric and metallic regimes of the ENZ i.e. for $|\lambda_{ENZ} - \lambda_{em}| > 50$ nm. Within this spectral regime increased material damping (γ) enhances radiated power rather than attenuating it and quenches the characteristic minimum at $\lambda_{ENZ} = \lambda_{em}$. Transmission through a media may be understood in terms of its optical dispersion, photon density of states (PDOS) and the group velocity (v_g), as shown in fig. 3b-d for various γ . The grey bands demarcate the spectral range 1600 ± 10 nm, which is investigated in the later sections. The dispersion plots in fig. 3b attest to the paucity in \vec{k} values for $\omega/\omega_z \leq 1$ i.e., in the ENZ and metallic regimes, where $\omega_z = 2\pi c/\lambda_{ENZ}$. The PDOS decreases significantly as

the ENZ media transitions from a dielectric to metallic regime, with a notable reduction at $\omega/\omega_z = 1$, as shown in fig. 3c. Note that with increasing γ , both the available \vec{k} and the PDOS increases for $\omega/\omega_z \leq 1$ and a non-zero γ ensures non-zero \vec{k} and PDOS, thereby aiding transmission in this spectral regime. The spectral variation of v_g (fig. 3d) shows that v_g is an increasing function of ω , for $\omega/\omega_z > 1$, with a minimum at ω_z and increases again at lower frequencies ($\omega/\omega_z < 1$) such that $v_g/c > 1$. For $\gamma = 10^{10}$ Hz, $v_g/c = 0.044$ at ω_z , which is commensurate with the demonstrated limits for slow-light [40]. To summarize, at $\omega/\omega_z \simeq 1$ minimal light couples into the ENZ media due to the restricted \vec{k} values and reduced PDOS, and the light that couple propagates very slowly due to the low v_g [17, 23, 41]. As γ increases, the pronounced dip in v_g at $\omega/\omega_z = 1$ diminishes (see Fig. 3d inset), which commensurate with the behavior of radiated power in fig. 3a. When the dipole oscillates at the same frequency as ω_z , decoupling of spatial and temporal components of the electromagnetic field in the ENZ medium minimizes propagation, leading to a minimum in radiated power that is prominent for low γ . Higher γ partially restores the PDOS and increases the range of allowed \vec{k} , facilitating transmission through the ENZ medium. The spectral window around λ_{ENZ} resembles an optical band gap, characterized by a low PDOS and reduced v_g . As $\omega/\omega_z \gg 1$, v_g eventually saturates to the phase velocity, as depicted in Fig. 3d. The minimum in v_g at ω_z and its superluminal values for $\omega/\omega_z < 1$ originate from the dispersive nature of the ENZ system, i.e., $n(\omega)$ and $dn/d\omega$ that ultimately becomes negative, as shown in SM fig. S6b [37]. Superluminal values of v_g [40, 42] has been investigated in the context of “fast-light media” and shown not to violate relativistic causality with the understanding that the velocity of actual information transfer is slower than v_g and does not exceed the value of the speed of light in vacuum [43]. Absence of radiative modes in the ENZ spectral regime around λ_{ENZ} , in materials like ITO, CdO etc., and the tunability of λ_{ENZ} via their free carrier density can be exploited to dynamically modulate their optical properties, between high and low transmissive states. These intriguing properties of unbounded ENZ materials, as discussed

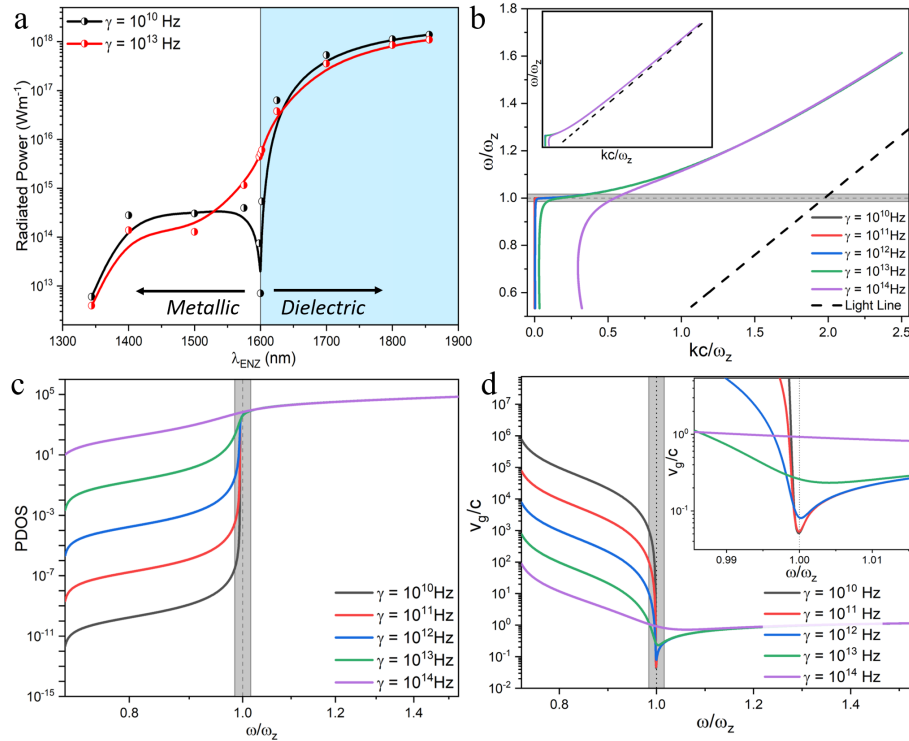


FIG. 3. Properties of ENZ media for different values of the damping factor γ . (a) Radiated power from a point dipole embedded in an unbounded ENZ media. (b) Photon dispersion relation, inset: expanded range demonstrating asymptotic convergence to the light line in the ENZ media for $\omega \rightarrow \infty$. (c) Photon density of states and (d) spectral variation of v_g/c , inset: variation near ω_z . Grey band denotes the spectral range 1590 - 1610 nm.

earlier, are retained in bounded thin-film configurations, enabling their practical application in radiation modulation. Here, we explore device architectures that leverage the dynamic tunability of electronic ENZ thin films for on-chip signal modulation and directional beam-steering applications.

B. Controlling Transmittance of an ENZ thin film

Towards practical realization of ENZ based devices, we consider the case of an emitter *embedded* behind an 5 nm thick ENZ thin film on a transparent substrate (SiO_2) as shown in the schematic in the inset of fig. 4a. The dipole oriented horizontally radiates at $\lambda_{em} = 1600$ nm and the ENZ thinfilm is characterised by the parameters as before, with $\gamma = 10^{10}$ Hz and a variable N_c . Power radiated by the emitter, passing through the substrate and the ENZ film is detected at the top boundary of the simulation domain and its variation with λ_{ENZ} is shown in fig. 4a. The radiated power reaches a minima when $\lambda_{ENZ} = \lambda_{em}$ with an FWHM of 1.7 nm. The radiation pattern around the dipole, for $\lambda_{ENZ} = 1575$ nm, 1600 nm and 1625 nm are shown in figs. 4b-d, which plots the magnitude of the Poynting vector ($|\vec{S}|$) on a logarithmic scale. In spite of the ultrathin thickness of the ENZ film, the radiation pattern is highly localized when

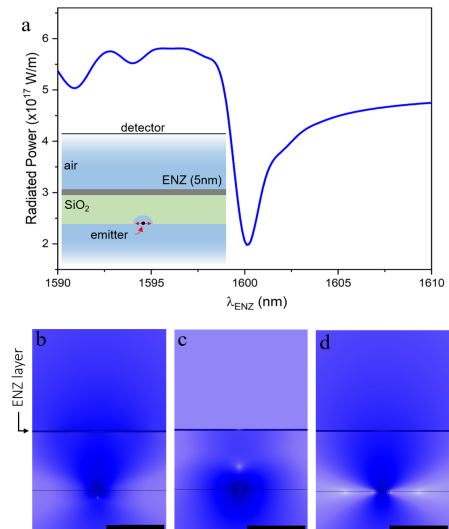


FIG. 4. (a) Radiated power transmitted through the ENZ film versus λ_{ENZ} . Inset: Schematic of the emission tailoring device with a 5 nm thick ENZ layer on top of a SiO_2 bulk with a point emitter placed beneath it. Magnitude of power flow ($|\vec{S}|$) plotted in log scale for (b) $\lambda_{\text{ENZ}} = 1575$ nm, (c) $\lambda_{\text{ENZ}} = 1600$ nm, and (d) $\lambda_{\text{ENZ}} = 1625$ nm. The emission wavelength of the point emitter is at $\lambda_{em} = 1600$ nm. Length of the black line shown in (b-d) is 200 nm.

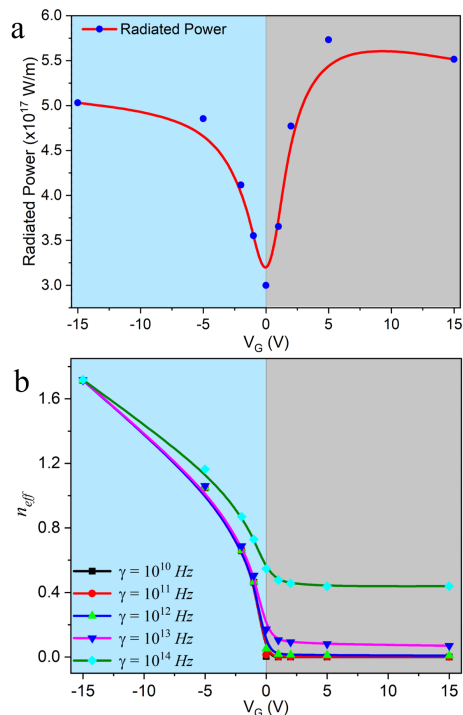


FIG. 5. (a) Radiated power transmitted through the ENZ film for $\gamma = 10^{10}$ Hz and (b) effective refractive index (n_{eff}) of the ENZ film for different γ versus V_G at $\lambda_{em} = 1600$ nm. The λ_{ENZ} for unbiased condition is 1600 nm.

$\lambda_{ENZ} \approx \lambda_{em}$ as shown in fig. 4c, with minimum transmission. As λ_{ENZ} shifts away from λ_{em} , transmission across the ENZ layer increases and is comparable across both the dielectric and metallic regimes investigated here. The high transmission in the metallic regime of the ENZ is surprising and occurs under the action of the ENZ thin-film's dispersion, finite loss and the film thickness being far smaller than the wavelength of radiation and the skin depth. As discussed earlier, for free-carrier ENZ systems, the λ_{ENZ} is tunable via its inverse proportionality to $\sqrt{N_c}$ [14, 38, 44, 45] and in such systems $N_c \simeq 10^{25} - 10^{27}/\text{m}^3$. The model in the inset of fig. 4a is modified to include a transparent insulator and top gate over the ENZ film to allow modulation of N_c , and thus λ_{ENZ} , by the application of a gate bias (V_G).

Variation in power transmitted across an ENZ thinfilm with V_G is shown in fig. 5a, which is minimum at $V_G = 0$ V due to the non-radiative modes of the ENZ. The carrier density of the film ($N_c = 6 \times 10^{26}/\text{m}^3$) is chosen such that its $\lambda_{ENZ} = 1600$ nm, matching the λ_{em} of the emitter at zero gate bias. Under positive (negative) V_G , accumulation (depletion) of electrons in the ENZ thin film results in a blue (red) shift of the thinfilm's effective λ_{ENZ} , making its response metallic (dielectric) at $\lambda_{em} = 1600$ nm. Variation of V_G between ± 15 V results in N_c modulation over 2 orders in magnitude at the interface, creating depletion and accumulation widths of ($w \simeq$) 3 nm and 1 nm, respectively, as shown in SM fig.

S4 [37]. The spatially varying $N_c(w)$ within the ENZ film changes the local \tilde{n} , the real and imaginary parts of which are shown in SM fig. S5 [37], for various values of V_G and γ . See SM section S2.2 for further details [37]. The effect of V_G induced N_c modulation on the optical properties of the film may be understood in terms of an effective refractive index n_{eff} at 1600 nm, spatially averaged across the cross-section of the ENZ thinfilm, as shown in fig. 5b. The similarity of this variation with the $n - \omega$ plot for an ENZ system shown in SM fig. S6a [37] is notable, demonstrating that changing V_G is akin to probing the different optical regimes of the ENZ film at a fixed emitter wavelength. Increase in radiated power for negative V_G , i.e., depletion, is expected, since the ENZ film behaves as a dielectric at 1600 nm, with its reduced N_c and thus a red-shifted effective λ_{ENZ} . Under positive V_G the electron accumulation layer blue-shifts the effective λ_{ENZ} and the ENZ behaves like a metal at 1600 nm. For any given γ , the higher κ in the metallic regime has little effect due to the ultra thin nature of the film, as discussed before. Thus, V_G effectively controls power flow (transmission) across the ENZ layer demonstrating a straightforward method for modulating emission intensity from an underlying or embedded emitter. While the intensity modulation on-off ratio for the 5 nm film for $\gamma = 10^{10}$ Hz is around 50% as shown in fig. 5a, the modulation frequency will be determined by the temporal response of the gate and mobility of the carriers in the ENZ layer. Note that the effective on/off ratio of transmission i.e. intensity modulation via spectral tuning of λ_{ENZ} with λ_{em} is determined by the damping factor (γ) of the ENZ medium and its thickness. In the ENZ regime, particularly when $\epsilon' \approx 0$, the imaginary component (ϵ'') significantly contributes to \tilde{n} and thus controls transmission through the ENZ medium. Thus, crucial to achieving the full potential of ENZ materials is the development of ENZ materials with small γ . SM fig. S7a [37] illustrates variation in power transmitted through an ENZ film as the γ decreases from $10^{13} - 10^7$ Hz, reinforcing the adverse effect of increasing γ , which effectively introduces radiative modes near λ_{ENZ} . This is better understood in the context of the point emitter embedded in an unbounded ENZ media (SM Sec. S4) [37]. SM figs. S8a-e [37] shows the evolution of an iso-power surface of constant value (3×10^{21} W/m²) for increasing γ with $\lambda_{ENZ} = \lambda_{em}$. The background plots $|\vec{S}|$ in log scale and shows that as γ increases the iso-power surface enlarges, denoting higher propagation. Thus, as real part of the dielectric constant and the refractive index becomes smaller in the ENZ regime, the thickness of the ENZ thinfilm i.e., the optical path length becomes increasingly crucial in determining the transmitted power. SM fig. S7b [37] shows the variation in radiated power for ENZ film thicknesses ranging from 5 nm to 105 nm. SM fig. S7c-d [37] plots the radiated power on/off ratio $P(1590)/P(1600)$ as functions of $\ln(\gamma)$ and film thickness, highlighting the ability to modulate transmissive radiation in ENZ media by adjusting its carrier density and

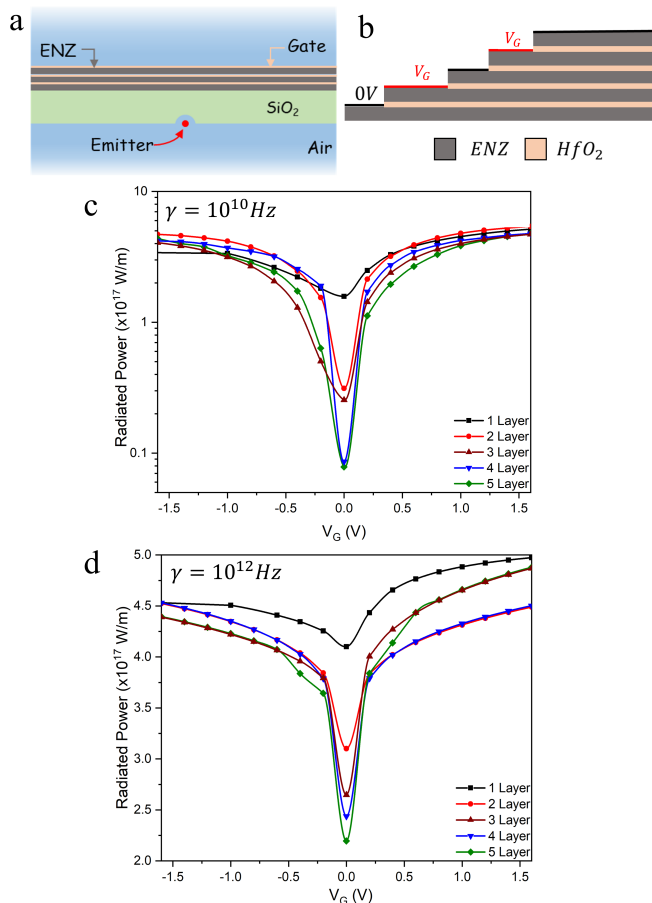


FIG. 6. (a) Multilayer ENZ device geometry for emission tailoring. (b) Zoomed up schematic of the multilayer gated system for different number of layers with (c) $\gamma = 10^{10}$ Hz and (d) $\gamma = 10^{12}$ Hz. The $\lambda_{em} = 1600$ nm and the non-gated $\lambda_{ENZ} = 1600$ nm.

thickness.

At λ_{ENZ} , free carrier ENZ materials have ϵ'' ranging from 0.001 to 0.6 that corresponds to γ between $10^{12} - 10^{14}$ Hz (table I), hence exhibit weak radiation attenuation, especially for ultra-thin films with thickness ~ 5 nm. While thicker films would show higher transmitted power on/off ratio, the efficacy of gating controlled tuning of λ_{ENZ} is limited, as screening of the gate field restricts the depletion/accumulation widths, typically around 2 nm of the interface [38, 46], thereby negating change in the \tilde{n}_{eff} . The problem can be mitigated by employing a multi-layer ENZ thin-film design, interleaved with an insulating dielectric, as shown in fig. 6. Here, multiple 5 nm thick layers of ENZ films are separated by a 1 nm thick dielectric gate layer (HfO_2), where each ENZ film can be gated with respect to the adjoining ENZ film. This multi-layer scheme negates the requirement of individual transparent gate electrodes, where alternate ENZ films are biased at 0V and V_G , allowing each ENZ film to either accumulate or deplete carriers, as shown

in fig. 6. SM fig. S10 [37] shows the spatial variation of electron density across a five layer stack of ENZ films with $N_c = 6 \times 10^{26}/\text{m}^3$ and $\lambda_{ENZ} = 1600$ nm. For V_G varying between ± 1.5 V, electrons accumulate and deplete in the alternating ENZ layers rendering them metallic or dielectric at 1600 nm. Since, transmission across the individual layers increase irrespective of the change towards metallic or dielectric, overall the stack becomes more transmissive for both positive and negative V_G . The efficacy of the multilayer gated structure is evidenced in the radiated power plots shown in fig. 6c-d for 1 - 5 layers of ENZ film, and $\gamma = 10^{10}$ Hz and 10^{12} Hz, demonstrating upto 50% intensity modulation for the lossy film. This architecture provides improved response compared to a single layer utilizing a multilayer gating scheme that removes the requirement of separate gate electrodes.

C. Beam steering

Leveraging the intensity modulation afforded by gating the ENZ thin film, we propose the design of an on-chip beam steering device. In this design, a single 5 nm thick ENZ thin film with λ_{ENZ} of 1600 nm is coated on a transparent substrate. The underside of the substrate features an extended array of dipole emitters, extending laterally over $10 \mu\text{m}$. As depicted in Figure 7a, here the gate electrodes form an array of interdigitated fingers with a width of 100 nm and a separation of 100 nm, extending along the x-direction over $10 \mu\text{m}$. A gate voltage, V_G is applied to a symmetric pair of gate electrodes, equidistant from the centre and separated by a distance of $2d$, with d varying from 100 nm to 5000 nm. Since the λ_{ENZ} of the film matches the emission wavelength of the dipoles, transmission across the ENZ film is minimum. However, once a non-zero V_G is applied at the pair of gates, the transmittance of the ENZ film below the gate electrodes is modified locally, which is practically independent of the sign of V_G , as shown in fig. 5a and fig. 6.

Fig. 7b plots the lateral variation in power detected by an extended detector placed along the top edge of the simulation domain, corresponding to $V_G = 0$ (red line) and $V_G \pm 1$ V for which the effective λ_{ENZ} of the gated windows change from 1600 nm to 1575 nm and 1625 nm. The $V_G = 0$ case denotes the lowest transmission state and increases locally as the windows are rendered dielectric or metallic at 1600 nm. The scheme mimics Young's double-slit experimental setup, with the exception that the entire ENZ film has non-zero transmission, which is highest at the regions with non-zero V_G . Consequently, the detected intensity profile at the top edge shows signatures of constructive and destructive interference, as shown in fig. 7c, for d varying from 2.5 - 5 μm . The device typically offers a ~ 2.5 times change in radiated intensity at the detectors while switching between the "on" state (red line) and the "off" state (black or blue line) in fig. 7b. Comprehending the interference pattern

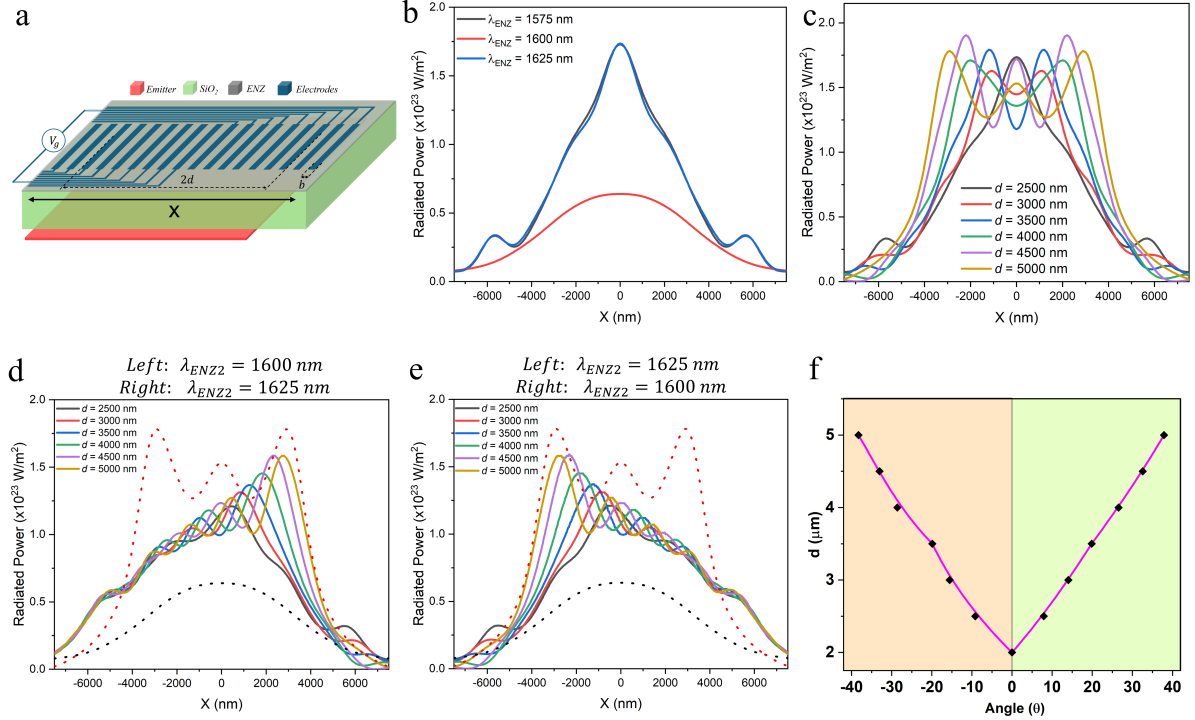


FIG. 7. (a) Schematic for effective beam steering. (b) Interference observed in radiated intensity at the top screen for different ENZ wavelength, with $d = 2500$ nm. Spatial variation in the radiated intensity for varying d , with the transmitting windows at (c) $\lambda_{ENZ} = 1625$ nm (d) Left $\lambda_{ENZ} = 1600$ nm and Right $\lambda_{ENZ} = 1625$ nm and (e) Left $\lambda_{ENZ} = 1625$ nm and Right $\lambda_{ENZ} = 1600$ nm, $b = 100$ nm and $\lambda_{em} = 1600$ nm (f) Quantifying beam steering in terms of angle of deviation in degrees.

is complex due to the non-trivial phase shift incurred by light at the interface of ultrathin ENZ films with $\text{Re}(\tilde{n})$ below one and has been discussed elsewhere [8].

The beam-steering capability is demonstrated by simulating the lateral variation of intensity at the detector array by applying $V_G = -1$ V to a single electrode at various d across the electrode array, as shown in figs. 7d-e. The black dotted lines correspond to zero bias applied at all gate electrodes and the red dotted lines represent the condition where two symmetric electrodes (separated by $2d = 10 \mu$ m) are biased at -1 V. Not only does the peak intensity shift laterally as the d of the single “on” electrode is increased, but it is accompanied by an increase in peak intensity. Results in figs. 7d-e show that the peak intensity detected at a distance 3.2μ m from the ENZ film laterally shifts by $\sim \pm 3 \mu$ m as the “on” electrode is shifted by $\pm 5 \mu$ m from the centre. This is equivalent to a beam steering capability of $\pm 38^\circ$, as shown in fig. 7f. Interference across the light transmitted through the entire ENZ thin film determines the intensity pattern at the detector array and also quantifies the transmission “on-off” ratio, which is a crucial parameter for achieving emission control and beam steering in the context of on-chip photonic devices. The design is readily scalable and can accommodate wider sources resulting in higher angular steering capability, upto $\pm 47^\circ$, as shown in SM

fig. S12a [37]. Such scalable architecture may be readily incorporated in on-chip photonic circuits to facilitate in optical communications, data routing and free-space optical interconnects.

IV. CONCLUSION

This study provides key insights into light-matter interactions in ENZ material, the role of material damping, and device engineering, demonstrating strategies for on-chip modulation of radiation intensity in the near IR spectral range. A simple device design is investigated where dynamic tuning of free-carrier density in 5 nm thick ENZ thinfilms via gating can modulate transmissivity as a function of gate voltage. The study highlights the role of carrier density and material damping in defining the efficiency (on/off ratio) of ENZ-based intensity modulators, where higher losses and restricted screening length limit the achievable on/off transmission ratio. To mitigate these limitations, a multilayer architecture is proposed that enhances the effective optical interaction length while maintaining dynamic tunability, offering a scalable solution for improving performance of practical ENZ-based photonic devices.

Later, dynamic beam steering is demonstrated utiliz-

ing spatially localized phase modulation enabled by selective control of ultrathin ENZ films. Future advancements in low-loss ENZ materials development and improved gating architecture will further enhance the efficiency and applicability of such strategies for integration in next-generation on-chip optical technologies.

ACKNOWLEDGMENTS

The authors acknowledge ISTEM, Government of India, for access to the COMSOL Multiphysics software and financial support from SERB, Government of India (No.CRG/2023/006878). AM acknowledges PhD fellowship from IISER Thiruvananthapuram.

-
- [1] S. Wang, P. C. Wu, V.-C. Su, Y.-C. Lai, C. Hung Chu, J.-W. Chen, S.-H. Lu, J. Chen, B. Xu, C.-H. Kuan, *et al.*, Broadband achromatic optical metasurface devices, *Nature communications* **8**, 187 (2017).
- [2] E. Cortés, F. J. Wendisch, L. Sortino, A. Mancini, S. Ezendam, S. Saris, L. de S. Menezes, A. Tittl, H. Ren, and S. A. Maier, Optical metasurfaces for energy conversion, *Chemical reviews* **122**, 15082 (2022).
- [3] V. Kalathingal, P. Dawson, and J. Mitra, Scanning tunnelling microscope light emission: Finite temperature current noise and over cut-off emission, *Scientific reports* **7**, 3530 (2017).
- [4] Z. Wang, V. Kalathingal, M. Trushin, J. Liu, J. Wang, Y. Guo, B. Özyilmaz, C. A. Nijhuis, and G. Eda, Up-conversion electroluminescence in 2d semiconductors integrated with plasmonic tunnel junctions, *Nature Nanotechnology*, 1 (2024).
- [5] S. Suresh, O. Reshef, M. Z. Alam, J. Upham, M. Karimi, and R. W. Boyd, Enhanced nonlinear optical responses of layered epsilon-near-zero metamaterials at visible frequencies, *Acs Photonics* **8**, 125 (2020).
- [6] M. Z. Alam, I. De Leon, and R. W. Boyd, Large optical nonlinearity of indium tin oxide in its epsilon-near-zero region, *Science* **352**, 795 (2016).
- [7] M. Silveirinha and N. Engheta, Tunneling of electromagnetic energy through subwavelength channels and bends using epsilon-near-zero materials, *Physical review letters* **97**, 157403 (2006).
- [8] B. Johns, S. Chattopadhyay, and J. Mitra, Tailoring infrared absorption and thermal emission with ultrathin film interferences in epsilon-near-zero media, *Advanced Photonics Research* **3**, 2100153 (2022).
- [9] S. Enoch, G. Tayeb, P. Sabouroux, N. Guérin, and P. Vincent, A metamaterial for directive emission, *Physical review letters* **89**, 213902 (2002).
- [10] K.-R. Choi, M. Kim, J. W. Wu, A. D'Aléo, and Y. U. Lee, Directive emission from polymeric fluorophore with epsilon-near-zero squaraine molecular film, *Nanophotonics* **12**, 2471 (2023).
- [11] W. D. Newman, C. L. Cortes, J. Atkinson, S. Pramanik, R. G. DeCorby, and Z. Jacob, Ferrell–berreman modes in plasmonic epsilon-near-zero media, *Acs Photonics* **2**, 2 (2015).
- [12] S. Krasikov, I. V. Iorsh, A. Shalin, and P. A. Belov, Levitation of finite-size electric dipole over epsilon-near-zero metamaterial, *physica status solidi (RRL)–Rapid Research Letters* **8**, 1015 (2014).
- [13] R. W. Ziolkowski, Propagation in and scattering from a matched metamaterial having a zero index of refraction, *Physical Review E* **70**, 046608 (2004).
- [14] B. Johns, N. M. Puthoor, H. Gopalakrishnan, A. Mishra, R. Pant, and J. Mitra, Epsilon-near-zero response in indium tin oxide thin films: Octave span tuning and ir plasmonics, *Journal of Applied Physics* **127** (2020).
- [15] J. Yang, H. A. Almossalami, Z. Wang, K. Wu, C. Wang, K. Sun, Y. M. Yang, and H. Ye, Direct observations of surface plasmon polaritons in highly conductive organic thin film, *ACS applied materials & interfaces* **11**, 39132 (2019).
- [16] M. Lobet, I. Liberal, L. Vertchenko, A. V. Lavrinenko, N. Engheta, and E. Mazur, Momentum considerations inside near-zero index materials, *Light: Science & Applications* **11**, 110 (2022).
- [17] I. Liberal and N. Engheta, Near-zero refractive index photonics, *Nature Photonics* **11**, 149 (2017).
- [18] I. Liberal, M. Lobet, Y. Li, and N. Engheta, Near-zero-index media as electromagnetic ideal fluids, *Proceedings of the National Academy of Sciences* **117**, 24050 (2020).
- [19] J. S. Hwang, J. Xu, and A. P. Raman, Simultaneous control of spectral and directional emissivity with gradient epsilon-near-zero inas photonic structures, *Advanced Materials* **35**, 2302956 (2023).
- [20] I. Liberal and N. Engheta, Nonradiating and radiating modes excited by quantum emitters in open epsilon-near-zero cavities, *Science advances* **2**, e1600987 (2016).
- [21] T. Gong, I. Liberal, M. Camacho, B. Spreng, N. Engheta, and J. N. Munday, Radiative energy band gap of nanostructures coupled with quantum emitters around the epsilon-near-zero frequency, *Physical Review B* **106**, 085422 (2022).
- [22] N. Engheta, Pursuing near-zero response, *Science* **340**, 286 (2013).
- [23] A. Ciattoni, A. Marini, C. Rizza, M. Scalora, and F. Biancalana, Polariton excitation in epsilon-near-zero slabs: Transient trapping of slow light, *Physical Review A* **87**, 053853 (2013).
- [24] M. H. Javani and M. I. Stockman, Real and imaginary properties of epsilon-near-zero materials, *Physical review letters* **117**, 107404 (2016).
- [25] A. D. Rakić, Algorithm for the determination of intrinsic optical constants of metal films: application to aluminum, *Applied optics* **34**, 4755 (1995).
- [26] M. Silvestri, A. Sahoo, L. Assogna, P. Benassi, C. Ferrante, A. Ciattoni, and A. Marini, Resonant third-harmonic generation driven by out-of-equilibrium electron dynamics in sodium-based near-zero index thin films, *Nanophotonics* (2024).
- [27] Y. Wang, A. Capretti, and L. Dal Negro, Wide tuning of the optical and structural properties of alternative plasmonic materials, *Optical Materials Express* **5**, 2415 (2015).
- [28] J. Kim, A. Dutta, G. V. Naik, A. J. Giles, F. J. Bezares, C. T. Ellis, J. G. Tischler, A. M. Mahmoud, H. Caglayan, O. J. Glembocki, *et al.*, Role of epsilon-near-zero sub-

- strates in the optical response of plasmonic antennas, *Optica* **3**, 339 (2016).
- [29] H. Kim, G. Kim, Y.-U. Jeon, W. Lee, B.-H. Lee, I. S. Kim, K. Lee, S. J. Kim, and J. Kim, Perovskite lanthanum-doped barium stannate: A refractory near-zero-index material for high-temperature energy harvesting systems, *Advanced Science* **11**, 2302410 (2024).
- [30] C. Han, J. Qiu, H. Liu, K. Chen, S. Liang, J. Yuan, M. Du, and H. Ye, Tunable enz properties in organic material pedot: Pss treated with different solutions, *Optical Materials Express* **14**, 1631 (2024).
- [31] Y. U. Lee, E. Garoni, H. Kita, K. Kamada, B. H. Woo, Y. C. Jun, S. M. Chae, H. J. Kim, K. J. Lee, S. Yoon, *et al.*, Strong nonlinear optical response in the visible spectral range with epsilon-near-zero organic thin films, *Advanced Optical Materials* **6**, 1701400 (2018).
- [32] N. C. Passler, I. Razzdolski, D. S. Katzer, D. F. Storm, J. D. Caldwell, M. Wolf, and A. Paarmann, Second harmonic generation from phononic epsilon-near-zero berreman modes in ultrathin polar crystal films, *Acs Photonics* **6**, 1365 (2019).
- [33] J. Li, S. Liu, S. Wu, W. Li, Y. Liu, and Z. Zhong, Broadband absorption based on multi-layered enz film: from directional to omnidirectional absorption, in *Journal of Physics: Conference Series*, Vol. 2548 (IOP Publishing, 2023) p. 012016.
- [34] R. Xu, I. Crassee, H. A. Bechtel, Y. Zhou, A. Bercher, L. Korosec, C. W. Rischau, J. Teyssier, K. J. Crust, Y. Lee, *et al.*, Highly confined epsilon-near-zero and surface phonon polaritons in srtio3 membranes, *Nature Communications* **15**, 4743 (2024).
- [35] J. D. Caldwell, A. V. Kretinin, Y. Chen, V. Giannini, M. M. Fogler, Y. Francescato, C. T. Ellis, J. G. Tischler, C. R. Woods, A. J. Giles, *et al.*, Sub-diffractive volume-confined polaritons in the natural hyperbolic material hexagonal boron nitride, *Nature communications* **5**, 5221 (2014).
- [36] Z. Jacob, Hyperbolic phonon-polaritons, *Nature materials* **13**, 1081 (2014).
- [37] See supplemental material at [url will be inserted by publisher] for details on finite element modelling and extended discussions on the effects of damping factor, .
- [38] A. Mambra, R. Pant, and J. Mitra, Dynamic tuning of enz region of ito and sensing using a tapered optical fiber, in *International Workshop on the Physics of Semiconductor and Devices* (Springer, 2021) pp. 229–236.
- [39] E. Feigenbaum, K. Diest, and H. A. Atwater, Unity-order index change in transparent conducting oxides at visible frequencies, *Nano letters* **10**, 2111 (2010).
- [40] P. W. Milonni, *Fast light, slow light and left-handed light* (CRC Press, 2004).
- [41] O. Reshef, I. De Leon, M. Z. Alam, and R. W. Boyd, Nonlinear optical effects in epsilon-near-zero media, *Nature Reviews Materials* **4**, 535 (2019).
- [42] J. D. Jackson and R. F. Fox, *Classical electrodynamics* (1999).
- [43] M. D. Stenner, D. J. Gauthier, and M. A. Neifeld, The speed of information in a ‘fast-light’ optical medium, *Nature* **425**, 695 (2003).
- [44] J. Karst, M. Floess, M. Ubl, C. Dingler, C. Malacrida, T. Steinle, S. Ludwigs, M. Hentschel, and H. Giessen, Electrically switchable metallic polymer nanoantennas, *Science* **374**, 612 (2021).
- [45] Y.-W. Huang, H. W. H. Lee, R. Sokhoyan, R. A. Pala, K. Thyagarajan, S. Han, D. P. Tsai, and H. A. Atwater, Gate-tunable conducting oxide metasurfaces, *Nano letters* **16**, 5319 (2016).
- [46] R. A. Maniyara, D. Rodrigo, R. Yu, J. Canet-Ferrer, D. S. Ghosh, R. Yongsunthon, D. E. Baker, A. Rezikyan, F. J. García de Abajo, and V. Pruneri, Tunable plasmons in ultrathin metal films, *Nature Photonics* **13**, 328 (2019).

Appendix A: Supplementary Material

1. Dielectric permittivity of ITO, CdO and PEDOT:PSS

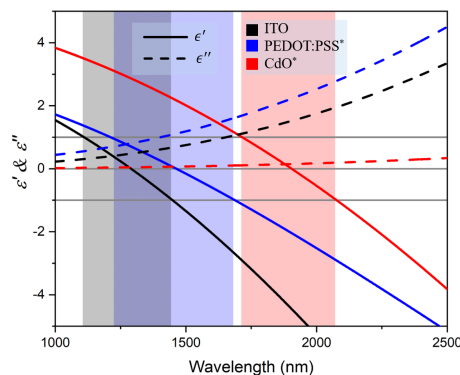


FIG. 8. Real (ϵ') and imaginary (ϵ'') part of dielectric permittivity for ITO, CdO and PEDOT:PSS plotted as a function of wavelength. The colored regions demarcate the ENZ regime i.e. the spectral regime within which $|\epsilon'| < 1$, for each material.

2. Finite element Method Modeling

All finite element simulations were carried out using the Wave Optics and Semiconductor modules of COMSOL Multiphysics (5.3a). The wave-optics simulations were performed with Perfectly Matched Layer (PML) boundary conditions applied around the simulation geometry. PML boundary condition is most preferred here since it allows to simulate open boundaries by fully absorbing outgoing wave, thus removing reflections from the boundary. A PML layer thickness ($1 \mu\text{m}$) of the order of excitation wavelength was used for maximum absorption at the boundary. The mesh density for ultra-thin (5 nm) ENZ films was optimized with free triangular pattern to have a mesh size ranging from 1 \AA to 0.1 \AA . On the other hand, while using semiconductor module to gate the ENZ layer, mapped mesh pattern with a geometric sequence distribution was used, since high mesh density ($<0.1 \text{ \AA}$) around the gate interface was essential to resolve the change in free carrier density and refractive index across depth of the ENZ layer. Other geometric domains were meshed with simple free triangular pattern and PML were meshed with mapped pattern. Fig.9 shows the two simulation geometry with the emitter embedded in unbounded ENZ media (fig.9a) and dynamic control of emission through ENZ media (fig.9b). The ENZ media under wave-optics module was defined using Drude model and the parameters used are as shown in table II. The point emitter was simulated using electric point dipole node in wave optics module with a dipole moment: $p = \omega \cdot 1 \times 10^{-10} [\text{A} \cdot \text{m}]$, oriented in x axis. The emitter is encapsulated in a vacuum bubble (dia: 50 nm) to save the solutions from diverging due to presence of source and sink at the same point. In the beam steering simulations a dipole emitter array was mimicked using surface current density node with $J = \omega \cdot 5 \times 10^{-5} [\text{A/m}]$.

Property	Value
High Frequency Permittivity	3.9
Free carrier Density	$6 \times 10^{26} \text{ m}^{-3}$
Effect mass of carrier	$0.35 m_e$
Scattering rate (γ)	$10^{10} - 10^{14} \text{ Hz}$

TABLE II. Material parameters defining ENZ media in Wave optics module. m_e is the free electron mass

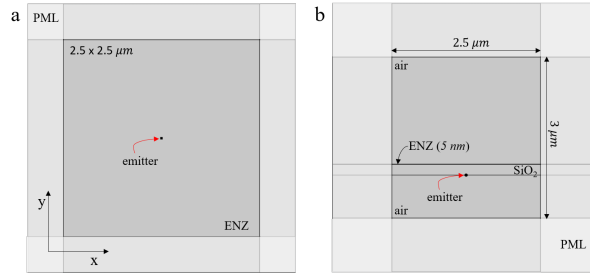


FIG. 9. Simulation geometry for (a) emitter embedded in Unbounded ENZ media, and (b) dynamic radiation control using ultra-thin film of ENZ.

a. Non-radiative modes

When, $\lambda_{em} = \lambda_{ENZ}$ and $\gamma = 10^{10} \text{ Hz}$, the dipole oscillator embedded inside the ENZ media mimics the \vec{E} profile of a electrostatic dipolar field, as shown in fig. 10. The \vec{E} still remains oscillating inside the vacuum bubble, it only shows the electrostatic nature in the ENZ media. The excitation of such a field profile is understood as non-radiative mode. The false color in the background corresponds to $\log(|\vec{E}|)$ as depicted by the colorbar.

b. Semiconductor Module

Thin insulated gate node of the semiconductor module and HfO_2 layer with 1 nm thickness was modelled to gate the ENZ media and Fermi-Dirac carrier statistic was used to solve for number density of majority carriers. The

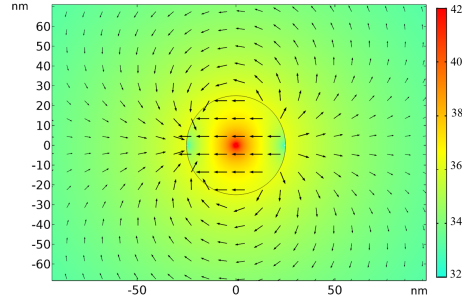


FIG. 10. Electrostatic dipolar field for $\lambda_{ENZ}=1600$ nm and $\lambda_{em}=1600$ nm

material parameters used to describe the ENZ and HfO_2 layer in semiconductor module is tabulated in table III. In semiconductor and wave-optics coupled simulations, the semiconductor module is first used to solve the variation in number density in the ENZ layer as a function of gate voltage (V_G). This simulated number density across the bulk of ENZ layer is fed into the Drude model which effectively calculates the refractive index ($\tilde{n}(x, y) = n + i\kappa$) across the bulk of ENZ media. This $\tilde{n}(x, y)$ is further used by wave-optics model to solve wave equations. Fig.11a and 11b shows the variation in the free-carrier number density for negative and positive (V_G), respectively. Similarly the 2D plots in fig.11c and 11d shows the variation in N_c across the whole bulk of ENZ media at -15 V and $+15$ V, respectively. These plots signify that $V_G = -15$ V creates a depletion width of ~ 3 nm and $V_G = +15$ V creates an accumulation width of ~ 1 nm. The real and imaginary part of refractive index (fig.12) of the ENZ media is derived from the simulated N_c (fig.11) with different material damping ($\gamma = 10^{10} - 10^{14}$ Hz).

Property	ENZ	HfO ₂
Relative permittivity	9.3	10
Band gap	3.5 eV	11 eV
Electron affinity	4.1 eV	0.1 eV
Effective Density of states (VB)	$1.0236 \times 10^{25} \text{ m}^{-3}$	-
Effective Density of states (CB)	$5.196 \times 10^{24} \text{ m}^{-3}$	-
Electron Mobility	$23 \text{ cm}^2 \text{ V}^{-1} \text{ s}^{-1}$	-
Hole Mobility	$1 \text{ cm}^2 \text{ V}^{-1} \text{ s}^{-1}$	-

TABLE III. Materials properties used in the semiconductor module

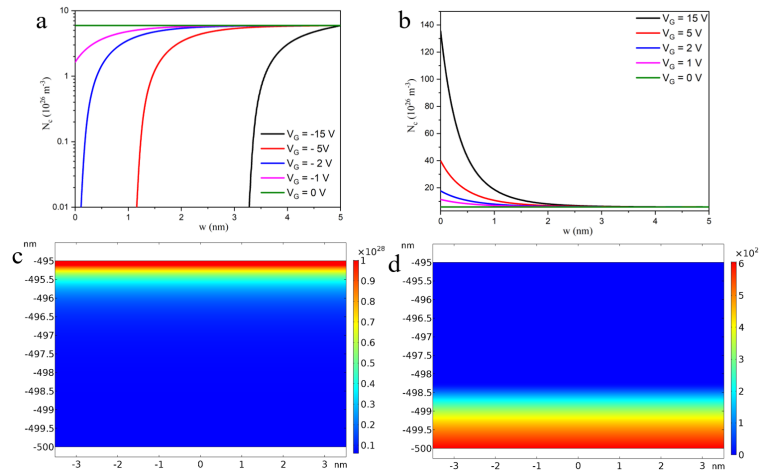


FIG. 11. Variation in number density (N_c) for (a) Negative and (b) Positive gate voltage. 2D plot shows depletion and accumulation width for (c) $V_G = -15$ V and (d) $V_G = 15$ V across the ENZ media.

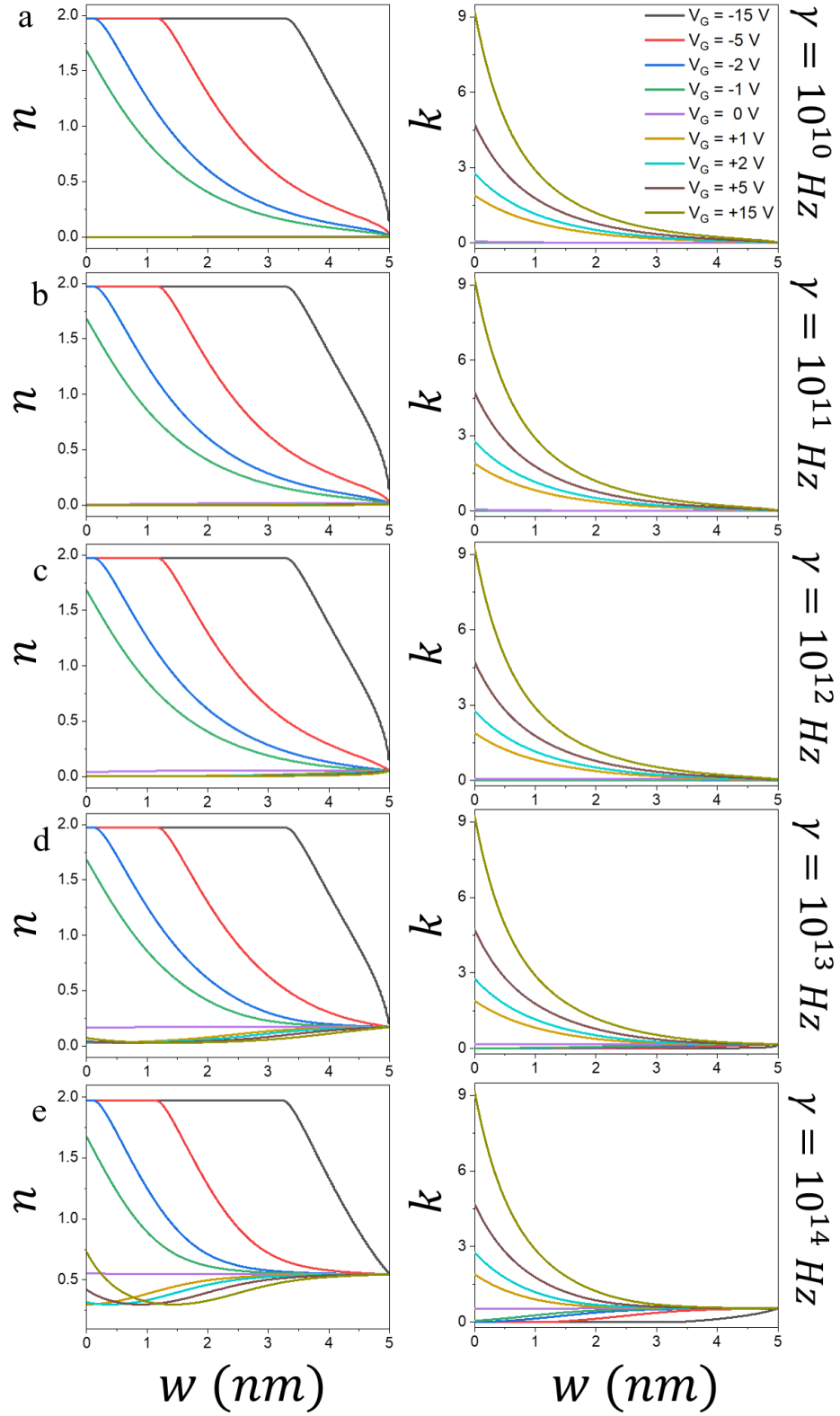


FIG. 12. Calculated n and κ across the depth of the ENZ layer for different γ .

3. Effect of γ and film thickness

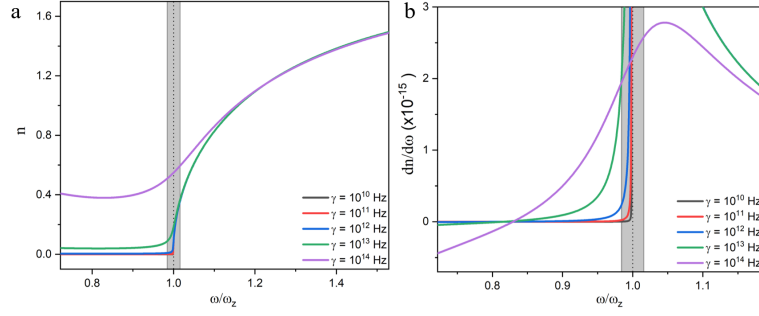


FIG. 13. (a) Real refractive index (n) and (b) $dn/d\omega$ as a function of ω for different γ .

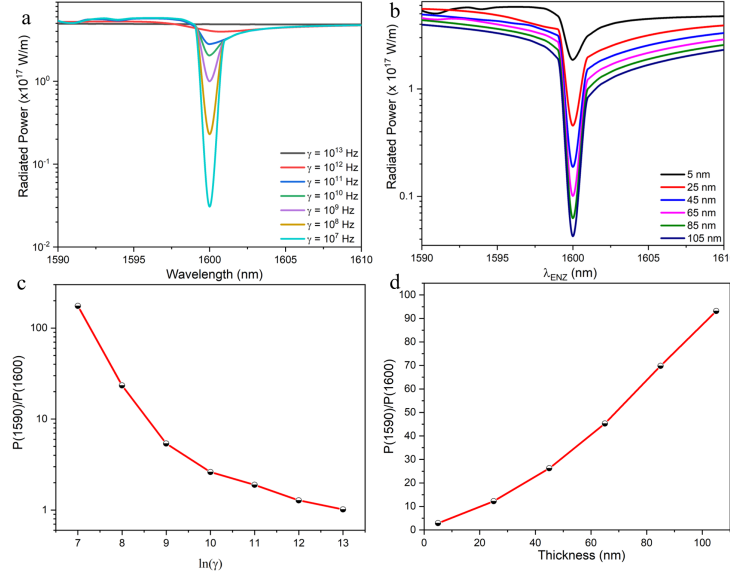


FIG. 14. Effect of radiated power as a function of (a) γ , for 5 nm thick film and (b) film thickness, for $\gamma = 10^{10}$ Hz. The ON-OFF ratio is calculated with $P(1590 \text{ nm})/P(1600 \text{ nm})$ for different (c) γ and (d) thickness of film

4. Effect of γ on Power flow in ENZ media

Power flow around a dipole embedded in an unbounded ENZ media with the λ_{em} matching λ_{ENZ} , exploring the role of γ is presented in figs. 15a-e. The colour map depicts a log scale plot of the magnitude of the Poynting vector ($|\vec{S}|$), with the green lines denoting iso-power flow contour of magnitude $3 \times 10^{21} \text{ W/m}^2$, for γ increased from $10^{10} - 10^{14}$ Hz. Fig. 15f plots $|\vec{S}|$ (in dB) as a function of distance from the dipole emitter. The plots show that for the dipole emitting at the λ_{ENZ} , power coupled into the ENZ media increases with increasing ENZ damping. Though the lowest power is coupled into the ENZ media for the smallest damping, radiation propagates less-dissipatively through the media compared to the case of higher γ . Hence, the impact of non-radiative modes at λ_{ENZ} are more pronounced for lower the γ . Alternatively, fig. 16a plots $|\vec{S}|$ for a fixed γ ($= 10^{10}$ Hz) and variable λ_{ENZ} . Again, the power coupling into the ENZ media is least when $\lambda_{ENZ} = \lambda_{em}$ and propagates less-dissipatively. For $\lambda_{ENZ} > \lambda_{em}$ the material behaves like a dielectric, resulting in higher power coupling with least dissipation, and for $\lambda_{ENZ} < \lambda_{em}$ the media behaves metallic, which again couples in relative higher power as compared to the case of $\lambda_{ENZ} = \lambda_{em}$ but the

propagation is significantly lossy. In the same scheme, fig. 16b plots power dissipation density ($P_D \approx \omega \epsilon'' |\vec{E}|^2$).

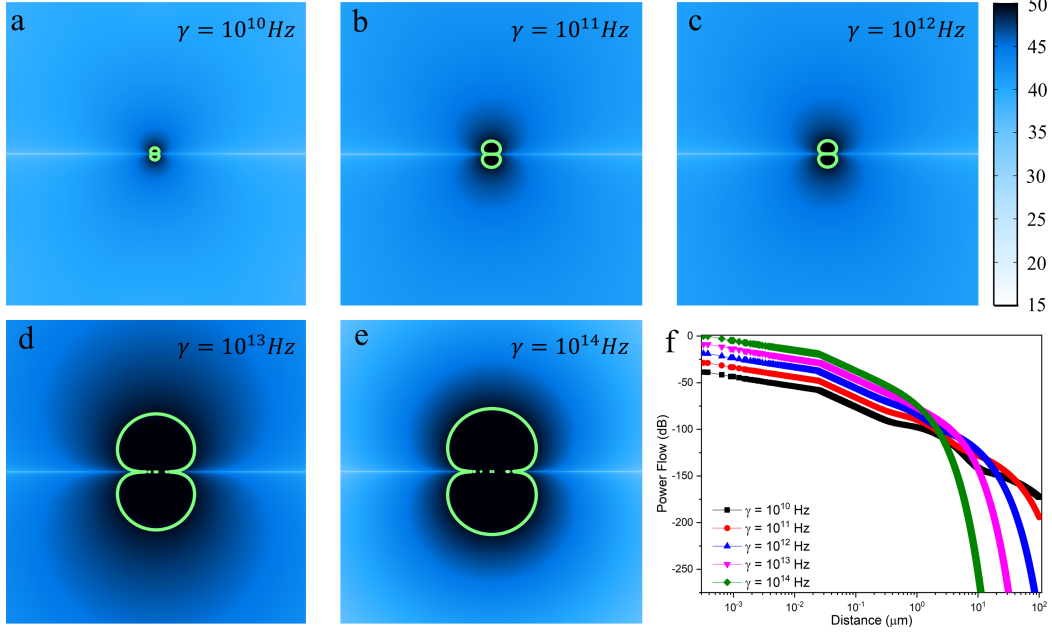


FIG. 15. $|\vec{S}|$ in log scale from a point dipole embedded in unbounded ENZ media with (a) to (e) increasing γ . Green contour shows an ISO power line at 3×10^{21} W/m². (f) Magnitude of Power in dB versus distance from the point dipole for different γ .

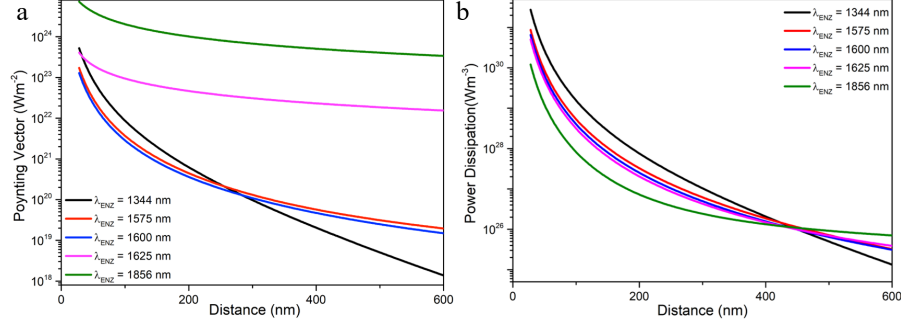


FIG. 16. (a) Power flow, $|\vec{S}|$ and (b) power dissipation density as a function of distance from the point source for different λ_{ENZ} and $\gamma = 10^{10}$ Hz.

5. Multi-layer architecture

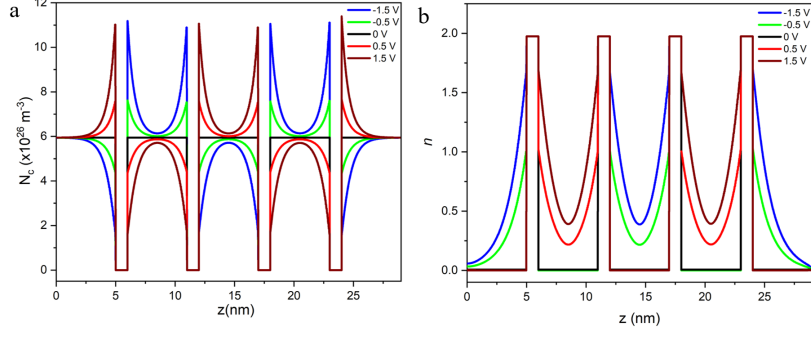


FIG. 17. Variation of (a) free carrier density, N_c and (b) real refractive index, n across the length of 5 layer structure as shown in fig. 9b (main paper), for various applied gate voltage V_G

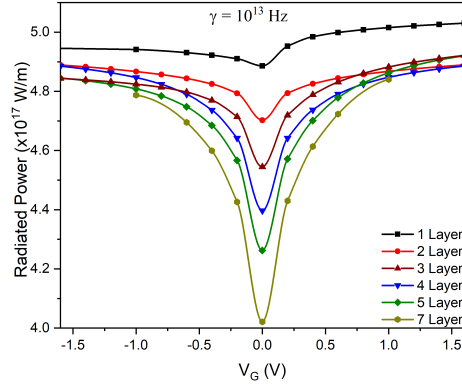


FIG. 18. Power radiated as a function of V_G for different number of layers. Here the materials loss is $\epsilon'' = 0.01$

6. Wider structure for increased angle of steering

The simulations demonstrating beam steering were performed with the lateral extent of the dipole array longer than the overall width of the digitated gate electrodes i.e. the maximum d . It implies that in real systems the illumination source is always larger than the tunable ENZ strip structures. Simulation results presented in fig. 19 show that the scheme is scalable i.e. the range of steering angle can be increased using wider array of electrodes and a commensurately wider source. The angular deviation increases to $\pm 47^\circ$ for the gate electrode array increased to $12 \mu\text{m}$.

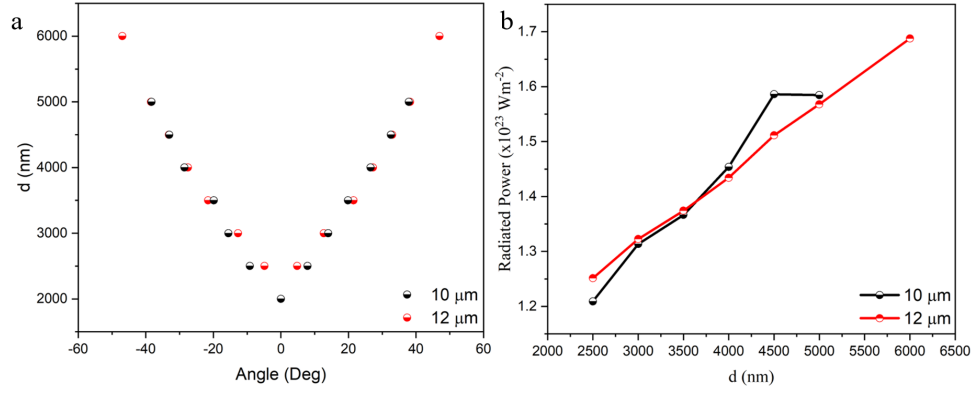


FIG. 19. (a) Angle of deviation (b) Maximum power radiated at steered angle as a function of d . $10 \mu\text{m}$ and $12 \mu\text{m}$ denotes the length of the dipole array